Cyclable Cu^I-O$_v$-Mn sites accelerate O$_2$ activation to enhance photo-driven catalytic oxidation performance

Yang Wang [a,b], Min Wang [a,b], Xixiong Jin [a,b], Bohan A [a,b], Bing Nan [d], Lina Li [d,*], Lingxia Zhang [a,b,c,**], Jianlin Shi [a,b]

[a] *Shanghai Institute of Ceramics, Chinese Academy of Sciences, 1295 Ding-xi Road, Shanghai 200050, PR China*
[b] *Center of Materials Science and Optoelectronics Engineering, University of Chinese Academy of Sciences, 19A Yuquan Road, Beijing 100049, PR China*
[c] *School of Chemistry and Materials Science, Hangzhou Institute for Advanced Study, University of Chinese Academy of Sciences, 1 Xangshan Sub-lane, Hangzhou 310024, PR China*
[d] *Shanghai Synchrotron Radiation Facility, Shanghai Advanced Research Institute, 239 Zhangheng Road, Shanghai, PR China*

ARTICLE INFO

ABSTRACT

Molecular oxygen activation (MOA) plays a crucial function in various oxidation reactions. Nonetheless, facile, continuous and efficient MOA remains challenging. Herein, we have successfully constructed recyclable Cu^I-O$_v$-Mn sites (O$_v$: oxygen vacancy) for MOA by incorporating Cu single atoms in MnO$_2$ matrix. The localized photogenerated electron at Cu^{II} site drives the generation of electron-rich Cu^I species and an adjacent photoinduced O$_v$, which possesses stronger O$_2$ affinity and affords a durable O$_2$ activation site. The Cu^{II}/Cu^I cycle accelerates the separation of charge carriers to supply adequate photogenerated electrons and assures the renewability of photoinduced O$_v$, thus realizing rapid and sustained O$_2$ activation and generating abundant monatomic oxygen ions (O$^-$). Consequently, Cu-MnO$_2$ catalyst performed extraordinarily high activity in O$_2$-involved reactions. For instance, in toluene oxidation, toluene conversion reached as high as 96 %, comparable to that on the state-of-the-art supported Pt catalysts. This work will bring more possibilities for modulating the O$_2$-involved oxidative reactions.

1. Introduction

Molecular oxygen (O$_2$) is an abundant and cheap oxidant in varieties of oxidation reactions for pollutant purification, energy conversion, chemical synthesis and so on [1,2]. Unfortunately, the inert triplet state of O$_2$ renders it difficult to react directly with other singlet molecules due to spin-forbidden property [3]. To break down this barrier, O$_2$ molecules need to be activated to reactive oxygen species (ROS) by changing spin state to singlet state (such as ^{1}O$_2$), or filling electron to antibonding π* orbital weakening O-O bond (such as O$_2^-$ and O$_2^{2-}$) [4,5]. Efficient activation of molecular oxygen has always remained a great challenge for decades.

It is widely believed that surface oxygen vacancy (O$_v$) is an important site for O$_2$ activation. O$_v$ can afford a specific unsaturated site for O$_2$ adsorption, and accelerate electron transfer from catalyst surface to the adsorbed O$_2$ molecule, thus accomplishing O$_2$ activation [6,7]. However, during oxidation reaction, O$_v$ is apt to be filled by the high

concentration of O$_2$, terminating the continuous O$_2$ activation ability. Single-atom catalysts (SACs) provide another possibility for O$_2$ activation, and their unsaturated coordination structure and electron transfer between the isolated atoms and supports are conducive to the adsorption and activation of O$_2$ molecules [2,8]. But the competitive adsorption of reactants/intermediates usually greatly hinders the O$_2$ activation capability of SACs [2,9–11]. Dual-atom catalysts (DACs) are expected to address this problem through the synergy of two adjacent sites. For instance, Zhang's group[12] developed Fe dual atom sites on MnO$_2$, which were believed to activate O$_2$ via an active intermediate species Fe (O=O)Fe. DFT calculations showed that Fe dual atom sites exhibited stronger O$_2$ activation performance than surface O$_v$. Nevertheless, the controllable synthesis and accurate characterizations of such DACs remain great challenges for most researchers. Towards this end, it is still indispensable to construct new active sites by facile approaches for continuous and effective O$_2$ activation. More importantly, clarifying the distinct O$_2$ activation mechanisms in these new systems is vital to

---

* Corresponding author.
** Corresponding author at: Shanghai Institute of Ceramics, Chinese Academy of Sciences, 1295 Ding-xi Road, Shanghai 200050, PR China.
E-mail addresses: lilina@sinap.ac.cn (L. Li), zhlingxia@mail.sic.ac.cn (L. Zhang).

motivate the rational design of highly efficient oxidation catalysts.

Here in this work, we developed a recyclable O_2 activation center, photoinduced Cu^I-O_v-Mn site, on MnO_2 matrix and deeply explored the O_2 activation mechanism. Combining in-situ X-ray photoelectron spectroscopy (XPS) with in-situ electron spin resonance spectroscopy (ESR), we discovered the Cu single atom site underwent a reversible evolution of Cu^{II}-O-Mn to Cu^I-O_v-Mn under irradiation. The photoinduced O_v presented renewable O_2 activation capacity, not only breaking the suspension of O_2 activation mediated by conventional O_v but also exhibiting stronger O_2 activation ability. Meanwhile, the Cu^{II}/Cu^I cycle accelerates the separation of photogenerated electrons to advance O_2 activation. Hence, Cu^I-O_v-Mn site can directly break the O-O bond to produce abundant monatomic oxygen ions (O^-), remarkably boosting the photothermal catalytic oxidation performance.

2. Experimental procedures

2.1. Materials

Potassium permanganate ($KMnO_4$, AR), copper (II) acetate monohydrate (($CH_3COO)_2Cu\bullet H_2O$, AR), iron nitrate nonahydrate (Fe$(NO_3)_3\bullet 9 H_2O$, AR), cobalt nitrate hexahydrate (Co$(NO_3)_2\bullet 6 H_2O$, AR) and hydrogen peroxide aqueous solution (30% H_2O_2, AR) were purchased from Sinopharm Co., Ltd. 2-(N-morpholino) ethane sulfonic acid (MES, RG) was obtained from Adamas Reagent, Ltd. Toluene solution (AR) was purchased from Shanghai Lingfeng Chemical Reagent Co., Ltd.

2.2. Catalyst preparation

The preparation method of MnO_2 was described in our previous work [13]. In brief, 1.06 g of MES was dissolved in 60 mL of deionized water. Then 60 mL of $KMnO_4$ (0.53 g) solution was dropped to the above solution under stirring. After 48 h of stirring, the powder MnO_2 sample was collected by centrifuging, washed with deionized water and ethanol, and freeze-dried.

Cu-MnO_2 was fabricated via a simple defect engineering method. Briefly, 200 mg of MnO_2 powder was dispersed in 60 mL of deionized water under sonication. A certain amount (1.5, 3 and 4.5 mg) of ($CH_3COO)_2Cu\bullet H_2O$ was added to the above solution followed by stirring for 1 h. Then, 2 wt% H_2O_2 solution was poured into the above solution and stirred for another 1 h. Finally, the Cu-MnO_2 sample was obtained via centrifuging and freeze-drying. The samples were marked as x Cu-MnO_2, in which x represented the theoretical mass ratio of Cu. Besides, Fe-MnO_2 and Co-MnO_2 were also synthesized through the same route using Fe$(NO_3)_3$ and Co$(NO_3)_2$ as precursors, respectively.

2.3. Catalyst characterizations

Inductively coupled plasma atomic emission spectroscopy (ICP-AES) was used to measure the content of metal single atoms. The X-ray diffraction (XRD) patterns were collected by Rigaku D/Max 2200PC X-ray diffractometer with Cu Kα (λ = 0.154 nm) at a scan rate of 4 ° min^{-1}. The Micromeritics Tristar 3000 analyzer was used to record N_2 adsorption-desorption isotherms. The specific surface area was calculated by the Brunauer-Emmett-Teller (BET) model and pore size distribution was determined by the Barrett-Joyner-Halenda (BJH) method. The morphology of samples was characterized by scanning electron microscope (SEM, Hitachi SU9000) and transmission electron microscopy (TEM, FEI Tecnai G2 F20). The LabRAM HR Evolution spectrometer with the excitation of 532 nm was performed to obtain Raman spectra. The JEM-ARM300F microscope was operated to capture high-angle annular dark-field scanning transmission electron microscopy (HAADF-STEM) images. X-ray absorption spectroscopy (XAS) measurements were completed at the 14B2 beamline of the Super Photon ring-8 (SPring-8, Japan). X-ray photoelectron spectroscopy (XPS) measurements were conducted on a Thermo Scientific ESCALAB 250

spectrometer with an Al Kα radiation, setting C 1 s to 284.8 eV to calibrate the binding energies. The Bruker A300 spectrometer was employed to record electron spin resonance (ESR) spectroscopy. The Shimadzu UV-3600 spectrometer was performed to acquire UV-Vis absorption spectra. The photoluminescence (PL) spectra were obtained on a Hitachi F-4600 fluorescence spectrophotometer with an excitation wavelength of 370 nm.

Temperature-programmed reduction of hydrogen (H_2-TPR) and temperature-programmed desorption of oxygen (O_2-TPD) measurements were performed on AutoChem II 2920 analyzer with a thermal conductive detector (TCD). Prior to tests, 100 mg of catalyst was pretreated at 150 ℃ in He for 1 h, followed by cooling to 45 ℃. For H_2-TPR, 10 % H_2/Ar (50 mL min^{-1}) passed through the samples and the temperature rose to 600 ℃ at a rate of 10 ℃ min^{-1}. For O_2-TPD, the samples were exposed to 3 % O_2/He (50 mL min^{-1}) for 30 min, followed by purging with He for 30 min, and finally heated to 800 ℃ with a rate of 10 ℃ min^{-1} in He (50 mL min^{-1}). The signals were collected by a TCD.

The photoelectrochemical measurements were conducted on CHI 760e electrochemical workstation (Chenhua Instrument, Inc.) with a standard three-electrode system, in which Pt wire, Ag/AgCl and fluorine-doped tin oxide (FTO) conductive glass coated by catalysts were used as counter electrode, reference electrode and working electrode, respectively. The electrolyte was 0.2 M Na_2SO_4 aqueous solution. The working electrode was prepared as follow: 20 mg of sample was mixed with 40 mg of iodine followed by dispersing them into acetone. Then, the above solution was poured into a 20 mL beaker with two pieces of FTO glass. After employing a voltage of 10 V, a homogeneous film was produced followed by drying at 150 °C for 2 h. The electrochemical impedance spectroscopy (EIS) was tested in dark at a bias voltage of −0.4 V vs Ag/AgCl. The photocurrent was measured under irradiation of a xenon lamp and a bias voltage of 0.4 V vs Ag/AgCl.

The $^{18}O_2$ isotope-labeled experiment was executed on a Mass Spectrometer (Hiden HPR-20 DLS). Before testing, the sample was purged under the flow of Ar at 200 ℃ to clean up surface adsorbed $^{16}O_2$. After cooling, the sample was passed through by 6 % $^{18}O_2/Ar$ for 30 min. Then the signal of effluent $^{16}O_2$ (m/z = 32) was detected online under irradiation.

The in-situ Fourier transform infrared (FT-IR) spectra were recorded by a Nicolet iS10 spectrometer with an HgCdTe (MCT) detector. The catalyst was pretreated in N_2 at 200 ℃ for 1 h. For photothermal catalysis, the background spectra were collected at room temperature. For thermocatalysis, the background spectra were obtained at the thermocatalytic reaction temperature. Then, the gas mixture of C_7H_8 and air (or N_2) was introduced into the cell at a rate of 50 mL min^{-1} followed by spectrum collection every 5 min.

The in-situ Raman spectra were collected on a LabRAM HR EvolutionLab-HRDLS 20 equipped with a 532 nm laser. The sample was purged with N_2 at 200 ℃ for 1 h to remove surface impurities, followed by cooling to room temperature. Then the sample was saturated with O_2 by flowing 3 % O_2/He for 30 min. At last, a serious of Raman spectra were obtained under irradiation or heating.

2.4. Catalyst evaluation

2.4.1. Photothermal catalytic (PTC) performance

The catalytic performance of catalysts for toluene oxidation was evaluated on a continuous flow reactor. In each test, 100 mg of catalyst was used and a gas mixture with 300 ppm C_7H_8 in air was fed into the reactor at a flow rate of 50 mL min^{-1}. For water tolerance tests, 2.5 or 5 vol% H_2O vapors were introduced by passing the feed gas through a water saturator at a certain temperature. After reaching adsorption-desorption equilibrium, a Xe lamp (CEL-HX, 300 W) was turned on with a light intensity of 300 mW·cm^{-2}. An online gas chromatography (GC-9790II, Fuli, China), equipped with two flame ionization detectors (FID) and a methanation furnace, was used to monitor the inlet and outlet concentrations of C_7H_8 and CO_2. Toluene conversion and

mineralization ratio were calculated through the following equations:

Toluene conversion (%) = (C_{in} - C_{out}) / C_{in}

where C_{in} and C_{out} represent the toluene concentrations in the inlet and outlet gas, respectively. Mineralization ratio (%) = ($C_{CO_2}/7 \times C_{in}$) where C_{in} and C_{CO2} represent the toluene concentrations in the initial gas and the CO_2 concentration generated in the catalytic oxidation reaction.

2.4.2. Thermocatalytic (TC) performance

The thermocatalytic (TC) performance of catalysts was measured in a continuous fixed-bed reactor in dark. The reaction temperature was controlled by an electrothermal furnace and other reaction conditions were the same as in the section of Photothermal catalytic (PTC) performance.

2.5. Density functional theory (DFT) calculations

All structure optimizations were accomplished by the density functional theory (DFT). Physical wave functions were expanded in terms of numerical basis sets in DMol3. The Effective Core Potentials (ECP) [14] were treated in the calculations for Fe, Co, Cu, and Mn atoms, whereas H, C and O were used in the all-electron. The double numerical plus polarization (DNP) was used as the basis set, and basis file is 3.5. Orbital cutoff quality was set fine. The generalized gradient approximation
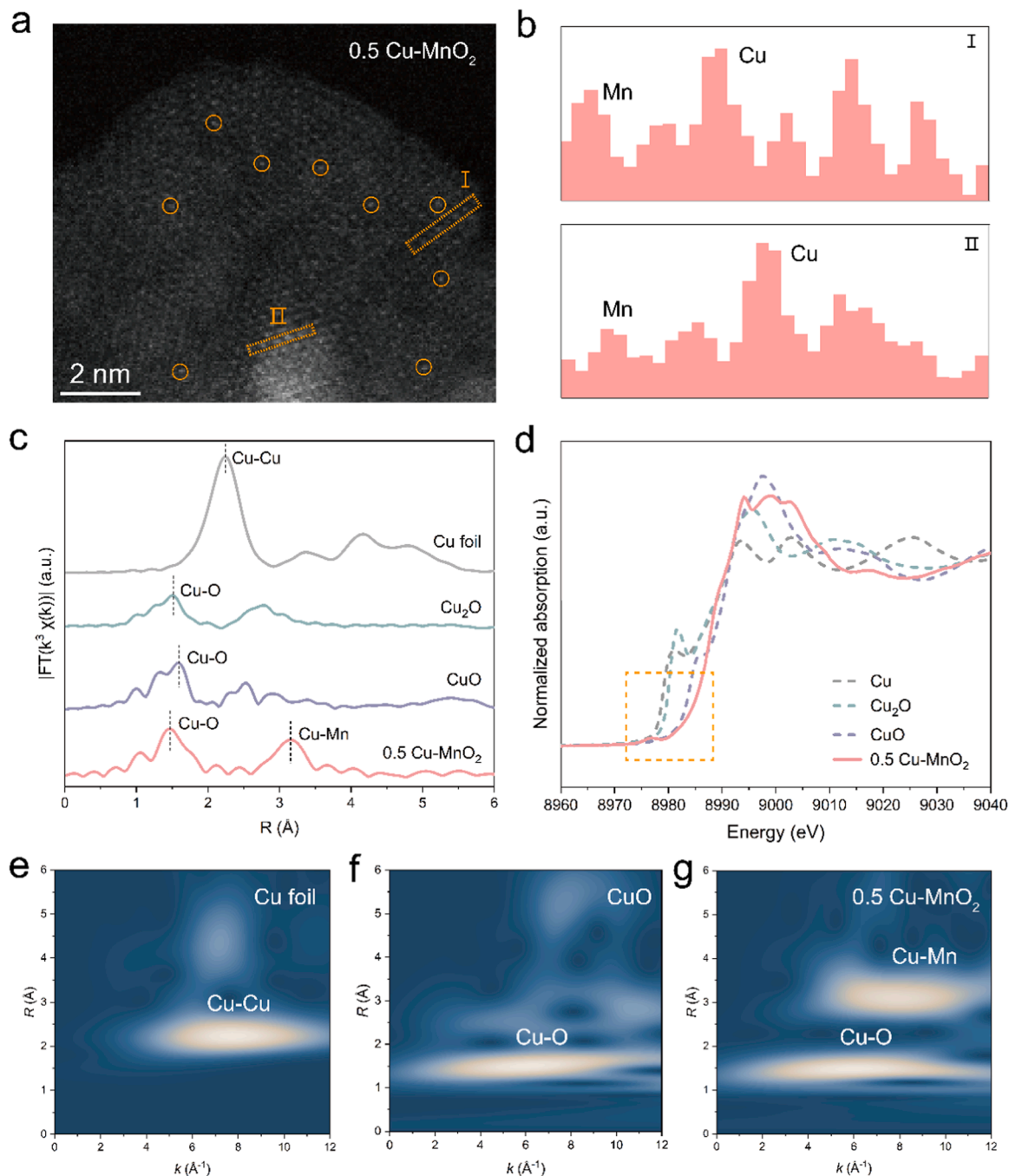

Fig. 1. (a) HAADF-STEM image of 0.5 Cu-MnO$_2$ and (b) the intensity profiles of the orange dotted area in (a). (c) The Cu K-edge Fourier-transformed EXAFS spectra and (d) the normalized XANES spectra of 0.5 Cu-MnO$_2$ and the reference samples (Cu foil, Cu$_2$O and CuO). Wavelet transforms of Cu K-edge EXAFS of (e) Cu foil, (f) CuO and (g) 0.5 Cu-MnO$_2$.

(GGA) with a Perdew–Burke–Ernzerh (PBE) method was performed as the exchange–correlation function [15]. Integration accuracy was set fine. A $3 \times 3 \times 1$ Monkhorst-Pack grid was chosen for the k-point meshes of Brillouin zone sampling [16]. The following convergence standards were established. The total energy is 10^{-5} Ha, the force is 0.002 Ha $Å^{-1}$, and the maximum displacement tolerance is 0.005 Å.

Further, the model of $4 \times 4 \times 1$ MnO$_2$ supercell for (001) surface was built from MnO$_2$. Such the Cu, Fe, Co atoms on MnO$_2$ (001) vacancy can remarkably enhance the binding capability. The adsorption energy (E) of all systems was written as $E = E_{MnO_2+o} - E_O - E_{MnO_2}$ where E_{MnO2+O}, E_O and E_{MnO2} represent the energy of bulk MnO$_2$(001) and organics, the energy of organics (such as toluene, benzaldehyde and benzoic acid), and the energy of MnO$_2$(001), respectively. With this definition, a negative value of E means a release of energy or stable adsorption on the surface.

3. Results and discussion

3.1. Structure and composition

All the XRD peaks of MnO$_2$ and Cu-MnO$_2$ are well indexed to the standard card (JCPDS 80–1098) of δ-MnO$_2$, with no diffraction peaks of Cu-containing species, indicating their high dispersion (Figure S1). Raman spectra show a weak band at 330 cm^{-1} assigned to the Cu-O band [17], demonstrating the successful introduction of Cu species (Figure S2). SEM and TEM images exhibit well-dispersed nanoflowers comprising two-dimensional nanosheets (Figure S3a, c and Figure S4a, c), featuring poor crystallinity as shown in Figure S4b and d. Due to the etching effect of H$_2$O$_2$ in the synthetic process, the structure of MnO$_2$ has partially collapsed (Figure S3b and d), resulting in increased specific surface area (Figure S5a, Table S3) and average pore size (Figure S5b, Table S3). The energy-dispersive X-ray spectroscopy (EDS) mapping images display a uniform distribution of Mn, O and Cu elements in the catalyst (Figure S6). HAADF-STEM image shows bright contrast spots located exclusively on the Mn atomic raw, validating that Cu single atoms lie in Mn vacancies (Fig. 1a and b). Further analysis for coordinational and electronic environments of Cu single atoms was executed by extended X-ray absorption fine structure (EXAFS) spectroscopy (Fig. 1c) and X-ray absorption near edge structure (XANES) spectroscopy (Fig. 1d). In EXAFS spectrum of 0.5 Cu-MnO$_2$, Cu-Cu bond is absent, strongly verifying the atomic dispersion of Cu, which is also identified by the visual results of wavelet transforms (Fig. 1e, f and g). Then, the fitting results reveal that the two peaks of 0.5 Cu-MnO$_2$ at 1.5 Å and 3.2 Å are ascribed to Cu-O bond and Cu-Mn bond [18], respectively (Figure S7), confirming the formation of the Cu-O-Mn structure, and the coordination number of Cu-O bond and Cu-Mn bond is 3.8 and 5.7, respectively (Table S4). Subsequently, XANES spectra present that the pre-edge feature of 0.5 Cu-MnO$_2$ is close to that of the CuO standard sample, suggesting that the valence state of Cu single atom is about +2. The first derivatives of the normalized XANES spectra are depicted in Figure S8. The spectrum of Cu^{2+} in CuO shows typical edge-energy features at 8977 and 8984 eV, corresponding to the 1 s→3d and 1 s→ 4p transition of Cu^{2+}, respectively [19,20]. They can both be viewed in the spectrum of 0.5 Cu-MnO$_2$, further implying the +2 state of Cu single atoms. The above results clearly illustrate that the isolated Cu atoms are anchored in the MnO$_2$ matrix as the Cu^{II}-O-Mn configuration, without compromising its crystal structure and morphology.

3.2. Catalytic performance

We evaluated the performance of the as-obtained catalysts on several typical O$_2$-involved oxidation reactions (such as toluene oxidation, CO oxidation and benzyl alcohol oxidation). Toluene is a toxic air pollutant, seriously harming the air environment and human health. Due to aromatic ring and steric hindrance of methyl groups[21], toluene

degradation at low temperature is more difficult than other common pollutants, such as CO, HCHO and benzene. So we employed toluene oxidation as a probe reaction to evaluate the photothermal catalytic performance of the as-prepared catalysts. All the Cu-MnO$_2$ catalysts show significantly enhanced activity compared to pure MnO$_2$, implying the crucial role of Cu single atoms in toluene oxidation (Figure S9 and 2a). 0.5 Cu-MnO$_2$ catalyst with Cu content of 0.48 wt% (Table S1) displays the highest toluene conversion of 96 % (Figure S9) and mineralization ratio of 95 % (Figure S10), which is comparable to or even better than that of the state-of-the-art supported Pt catalysts (Table S6). The pseudo-first-order reaction kinetic model was fitted to acquire kinetic constants, as shown in Fig. 2b. The kinetic constant of 0.5 Cu-MnO$_2$ is 1.9-fold that of MnO$_2$. The catalytic stability of 0.5 Cu-MnO$_2$ was further assessed (Fig. 2c). Notably, exposed in air for 71 days, the catalyst exhibits no decrease of activity in toluene conversion (II). Besides, even during the subsequent four cycles (III-VI), toluene conversion on it remains at $\sim$ 92 %. According to XRD patterns (Figure S11) and TEM images (Figure S12a), the used 0.5 Cu-MnO$_2$ catalyst maintains the initial phase and morphology. HRTEM (Figure S12b) and EDS mapping images (Figure S12c-f) detect no Cu aggregates. These ex-situ characterization results all prove that 0.5 Cu-MnO$_2$ catalyst is stable before and after the reaction. Water resistance is referred to as an obstacle to the practical application of catalysts [22,23]. Toluene oxidation was carried out under humidity conditions of 2.5 vol% and 5 vol% H$_2$O. The water vapor causes a slight increase in the catalytic activity of 0.5 Cu-MnO$_2$ (Fig. 2d) and 0.5 Cu-MnO$_2$ displays a very low performance decay of 1.3% in 24 h at 5 vol% H$_2$O (Fig. 2e). The surface-adsorbed H$_2$O can generate new active species, -OH and hydroxyl radical (·OH) (Figure S13), which can promote VOCs oxidation[13]. For CO oxidation (Figure S14), 0.5 Cu-MnO$_2$ catalyst shows a high CO conversion of 98 % under irradiation; and for the oxidation of benzyl alcohol (Figure S15), 0.5 Cu-MnO$_2$ catalyst can perform 93.8 % conversion of benzyl alcohol and nearly 100 % selectivity to benzaldehyde within 3 h under irradiation.

3.3. Photothermal synergetic effect

The surface temperature variation of the catalysts under irradiation of 300 mW·cm^{-2} was recorded by a thermocouple (Figure S16). The surface temperature of the catalysts rises rapidly to above 100 °C within 7 min, finally reaching the equilibrium temperature of 103 °C and 109 °C on MnO$_2$ and 0.5 Cu-MnO$_2$, respectively. These results verify that catalysts possess strong photothermal conversion ability. Then thermocatalytic (TC) performance tests were performed at the above equilibrium temperature to compare their photothermal catalytic (PTC) performance. At 110 °C and without catalysts, no toluene has been converted (Figure S17). On MnO$_2$ and 0.5 Cu-MnO$_2$, toluene conversion by thermocatalytic oxidation is 47 % and 55 %, respectively, as shown in Fig. 3a. Compared with TC performance, under irradiation, toluene conversion by photothermal catalytic oxidation on MnO$_2$ and 0.5 Cu-MnO$_2$ increases by 48 % and 74 %, respectively. Then, the PTC performance of 0.5 Cu-MnO$_2$ under varied light intensity and its TC performance at the corresponding equilibrium temperatures were evaluated (Figure S18b). The PTC performance of 0.5 Cu-MnO$_2$ increases rapidly with the light intensity ($<$ 300 mW·cm^{-2}), and toluene conversion is enhanced slightly when light intensity exceeds 300 mW·cm^{-2}. At weak light intensity, the TC activity is very poor due to the low surface temperature (Figure S18a), indicating the leading role of photocatalysis. Upon increasing light intensity, the equilibrium temperature of 0.5 Cu-MnO$_2$ rises linearly (Figure S18a), resulting in higher TC activity (Figure S18b), and thermocatalysis gradually dominates. Simultaneously, photocatalysis can accelerate the reaction kinetic of toluene oxidation (Figure S19). Therefore, it could be inferred that photothermal synergetic effect of the catalysts could contribute to the remarkably enhanced activity. Subsequently, the critical function of Cu single atoms was analyzed, taking PTC performance under light intensity of
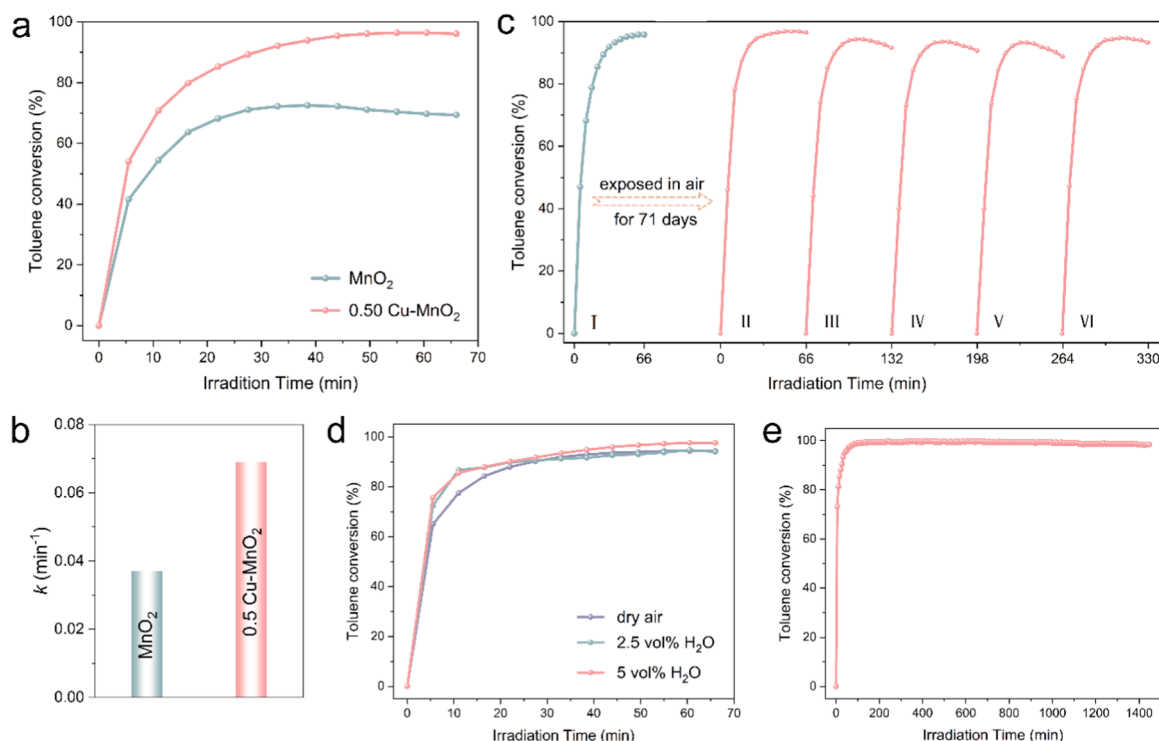
Fig. 2. (a) Photothermal catalytic activity of MnO_2 and 0.5 $Cu-MnO_2$ in toluene oxidation. (b) Kinetic constants of toluene oxidation over MnO_2 and 0.5 $Cu-MnO_2$. (c) Cyclic performance of 0.5 $Cu-MnO_2$ (The curves marked by II-VI represent the catalytic performance data of 0.5 $Cu-MnO_2$ after storage of 71 days.). (d) Effect of 2.5 vol% and 5 vol% water vapor on toluene conversion over 0.5 $Cu-MnO_2$. (e) Stability test of 0.5 $Cu-MnO_2$ at 5 vol% water vapor.
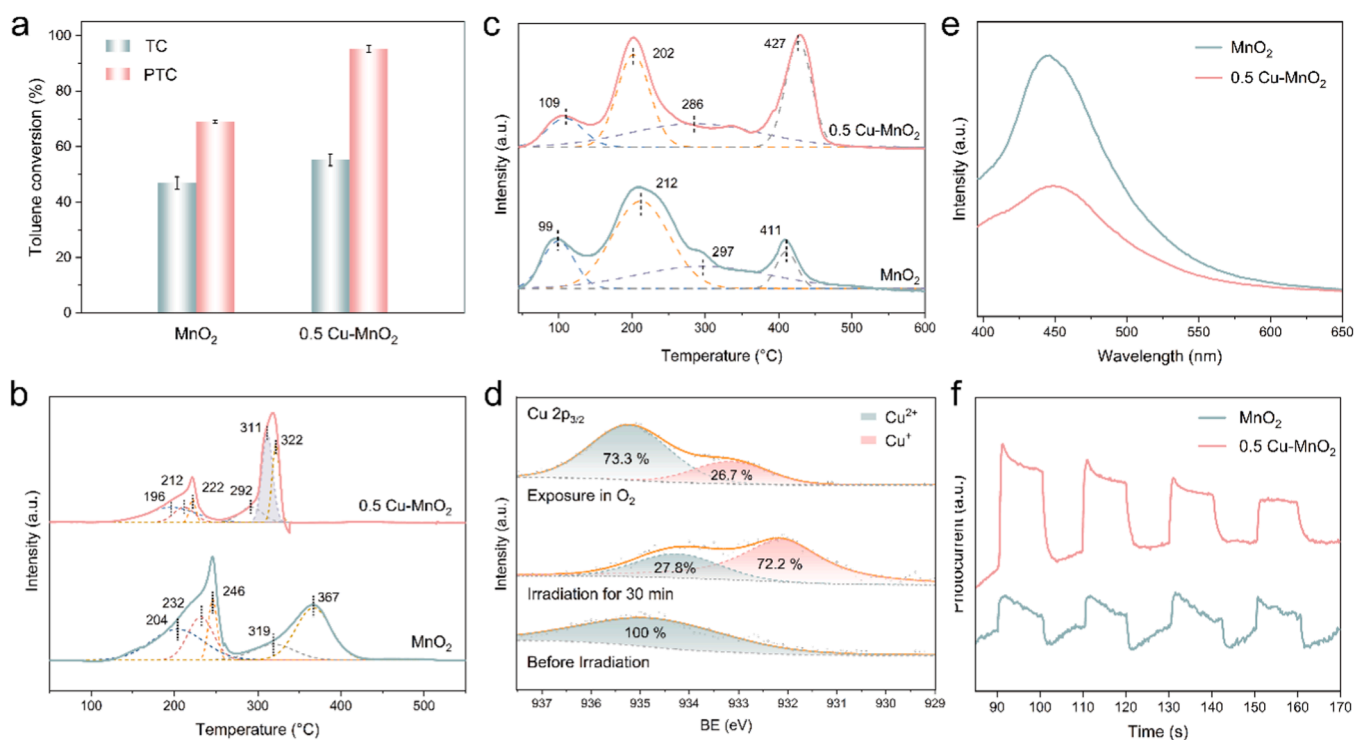

Fig. 3. (a) The photothermal catalytic (PTC) performance under irradiation of 300 $mW \cdot cm^{-2}$ and the thermocatalytic (TC) performance at the corresponding equilibrium temperature of MnO_2 and 0.5 $Cu-MnO_2$. (b) H_2-TPR and (c) O_2-TPD profiles of MnO_2 and 0.5 $Cu-MnO_2$. (d) In-situ Cu $2p_{3/2}$ XPS spectra of 0.5 $Cu-MnO_2$. (e) PL spectra and (f) photocurrent responses of MnO_2 and 0.5 $Cu-MnO_2$.

300 $mW \cdot cm^{-2}$ as an example. After the introduction of Cu single atoms, TC activity is enhanced slightly (Figure S20), only making up 31.6 % of the total increase in photothermal catalytic activity (Fig. 3a), implying that Cu single atoms contribute more to enhancing photocatalytic activity.

3.4. Enhanced thermocatalytic activity by Cu single atoms

The valence state of surface elements was analyzed by XPS. The Mn 3 s spectra exhibit that the average oxidation state (AOS) values of Mn decrease from 3.36 to 3.30 after incorporating Cu single atoms, suggesting more low-valence Mn species (Figure S21a). In Mn $2p_{3/2}$ spectra, the signals can be fitted into two peaks at 641.8 and 643 eV, assigned to Mn^{3+} and Mn^{4+}, respectively[24,25]. The proportion of Mn^{3+}/Mn^{4+} increases from 1.20 to 1.30 after Cu single atom introduction (Figure S21b and Table S5), in accordance with the result of Mn 3 s spectra. In O 1 s spectra, the percentage of surface adsorbed oxygen (O_{ads}) on 0.5 Cu-MnO$_2$ is higher than that on MnO$_2$ (Figure S22 and Table S5). These changes reflect more surface O_v on 0.5 Cu-MnO$_2$. ESR was implemented to confirm this speculation (Figure S23). As expected, the signal intensity of 0.5 Cu-MnO$_2$ assigned to O_v (g = 2.003) is stronger than that of MnO$_2$[26].

H$_2$-TPR profiles were recorded to test the reducibility of the as-prepared catalysts (Fig. 3b). MnO$_2$ catalyst displays five peaks at the region of 200–300 °C and 300–400 °C, which are ascribed to $Mn^{4+} \rightarrow Mn^{3+}$ and $Mn^{3+} \rightarrow Mn^{2+}$, respectively[27,28]. While for 0.5 Cu-MnO$_2$, a new peak at 311 °C belongs to the reduction of Cu species [29,30] and other peaks all show a shift to low-temperature, indicating its better reducibility. O$_2$-TPD measurements were executed to explore the desorption behavior of oxygen species on the catalysts (Fig. 3c). The fitting results reveal that the types of oxygen species have no change after incorporating Cu single atoms. The desorption peak of 0.5 Cu-MnO$_2$ at 427 °C is representative of surface lattice oxygen (O_{latt}) [31, 32] and its intensity is much stronger than that of MnO$_2$, signifying more active surface lattice oxygen in 0.5 Cu-MnO$_2$. Therefore, introducing Cu single atoms can improve the concentration of surface O_v and increase the activity of surface O_{latt} as well as low-temperature reducibility to bring about higher thermocatalytic activity.

3.5. Recyclable photoinduced Cu^I-O_v-Mn site to boost molecular oxygen activation

In-situ XPS spectra were collected to monitor the real valence of Mn and Cu in working conditions. As shown in Figure S24, the valence state
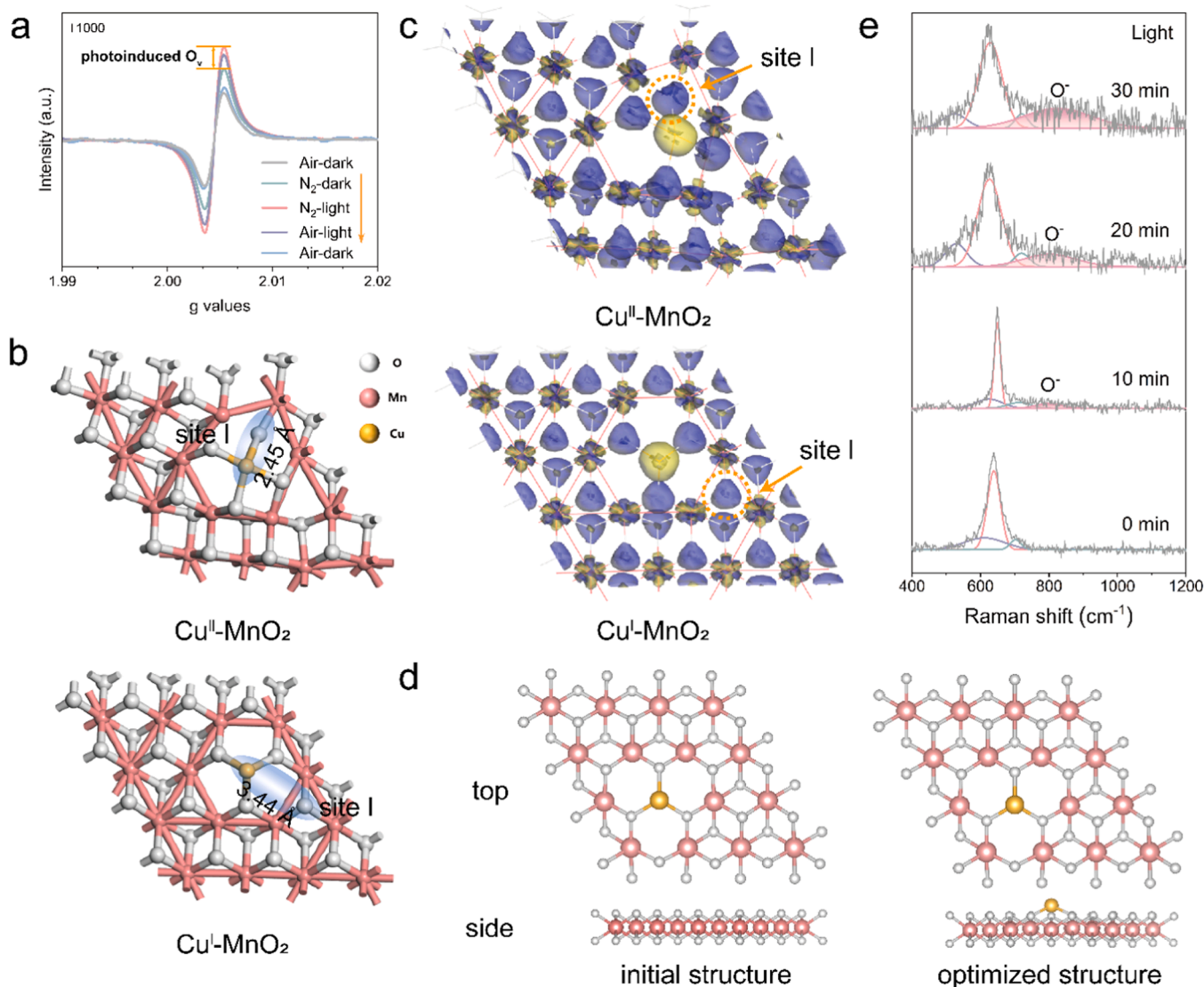

Fig. 4. (a) In-situ ESR spectra of 0.5 Cu-MnO$_2$ under different conditions. (b) The calculated Cu-O bond length and (c) charge density distribution in optimized Cu^{II}-MnO$_2$ and Cu^I-MnO$_2$ structures (blue and yellow areas represent charge accumulation and depletion, respectively). Note: at this moment, the Cu^{II} single atom is reduced to Cu^I single atom, and the O atom (site I) has left the equilibrium position, but not escaped from surface. (d) DFT model structures of Cu-MnO$_2$ with a photoinduced O_v (The O atom is divorced from surface and photoinduced O_v is created.). (e) In-situ Raman spectra of O$_2$ activation on 0.5 Cu-MnO$_2$ under irradiation.

of Mn has a subtle change. Amazingly, apparent variation can be noticed in in-situ Cu $2p_{3/2}$ XPS spectra (Fig. 3d). Before irradiation, the Cu $2p_{3/2}$ signal at 934.7 eV is attributed to Cu^{2+} [33]. After irradiation for 30 min, an additional peak at 932.1 eV emerges assigned to Cu^{+}, accounting for 72.2 % of the total Cu atoms [33]. Then, exposed in air, the proportion of Cu^{+} declines to 26.7 %, and the major valence value of Cu returns to +2. It can be deduced that Cu single atoms have been reduced to Cu^{+} by trapped photogenerated electron (e^{-}), then Cu^{+} is oxidized to initial Cu^{2+} by O_2, achieving a reversible Cu^{II}/Cu^{I} cycle. To figure out the effect of the reversible Cu^{II}/Cu^{I} cycle on light absorption property and charge carrier kinetics of the as-prepared catalysts, UV-Vis absorption spectra, PL spectra, photocurrent and EIS spectra were analyzed. As depicted in Figure S25, the as-synthesized catalysts exhibit strong light absorption ability in the visible and near-infrared light region, and light absorption increases after the introduction of Cu single atoms. PL spectrum of 0.5 Cu-MnO$_2$ shows the weaker emission intensity at 450 nm, testifying facilitated charge carrier separation (Fig. 3e). For EIS Nyquist plots, the smaller radius of 0.5 Cu-MnO$_2$ can prove lower charge transfer resistance and improved separation efficiency of carriers (Figure S26). These results are well consistent with photocurrent responses in Fig. 3f. 0.5 Cu-MnO$_2$ appears a strengthened photocurrent signal compared with MnO$_2$. Consequently, the reversible Cu^{II}/Cu^{I} cycle can accelerate electron extraction to realize efficient charge carrier separation and migration.
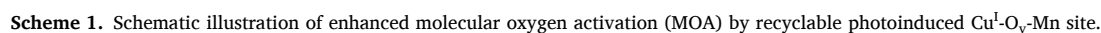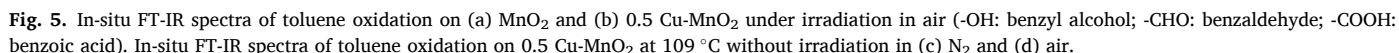
The vicinal coordination environment variation of the Cu single atoms caused by the Cu^{II}/Cu^{I} cycle was investigated by in-situ ESR under different conditions (Fig. 4a). First, 0.5 Cu-MnO$_2$ catalyst was purged with N_2 for 30 min and the signal intensity of O_v increased, indicating that adsorbed oxygen-containing compounds were removed to expose surface O_v. Then under irradiation in N_2, the signal further increased with irradiation time (Figure S27). When the light was turned off, the concentration of O_v returned to the initial value. So, it is supposed that irradiation can trigger the generation of new O_v, defined as photoinduced O_v. While for MnO$_2$, the amount of O_v has no obvious change under irradiation in N_2 (Figure S28), implying that the generation of photoinduced O_v highly relies on the Cu^{II}/Cu^{I} cycle. Subsequently, the main cause of photoinduced O_v was decoded. Firstly, the variation of Cu-O bond arisen from the reduction of Cu^{2+} was revealed by DFT calculations. The transformation of Cu^{2+} to Cu^{+} leads to the local lattice distortion around Cu atom by elongating Cu-O bond (site I) from 2.45 Å to 3.44 Å (Fig. 4b) and the reconstruction of surface electron distribution to make the O atom (site I) transfer partial electron to neighboring metal atom (Fig. 4c); accordingly, Cu-O bond (site I) is weakened and O atom (site I) is more likely detached from surface. Next, photogenerated h^{+} may participate in the production of photoinduced O_v by oxidizing surface oxide ions (O^{2-})[34,35]. After adding Na$_2$C$_2$O$_4$ into 0.5 Cu-MnO$_2$ to quench h^{+}, photoinduced O_v has been clearly suppressed (Figure S29). Furthermore, the evolution of lattice oxygen was traced by a mass spectrometer (Figure S30). In a flow of 6 % $^{18}O_2$/Ar, an increased $^{16}O_2$ signal was detected after irradiation, indicating the conversion of lattice O^{2-} to O_2. Hence, with the dual stimulations of the Cu^{II}/Cu^{I} cycle and h^{+}, loose lattice oxygen adjacent to Cu atom is prone to escape from the catalyst surface to generate photoinduced O_v and release O_2 (Figure S31).

After feeding air, the concentration of photoinduced O_v dropped slightly. It can be inferred that oxygen species derived from O_2 activation could refill photoinduced O_v, and the photoinduced O_v would reach a dynamic balance between its generation and replenishment by oxygen species. Next, the adsorption process of O_2 was investigated. The two possible pathways for the refilling of photoinduced O_v are considered as follow: one path is that O_2 is first adsorbed on the electron-rich Cu^{+} site, and then activated oxygen species spontaneously migrate to photoinduced O_v; the other one is that O_2 is directly adsorbed on the photoinduced O_v, followed by its activation by photogenerated e^{-}. DFT calculations were carried out to determine the preferable pathway. The optimized model structures of Cu-MnO$_2$ show that Cu atoms

spontaneously migrate from in-plane to out-plane when a bonded O atom gets away from the surface (Fig. 4d). If O_2 adsorption on the Cu site occurs, the generated active oxygen species must transfer to new O_v in the opposite direction by crossing a layer of MnO$_6$ octahedra. But it is infeasible from the point of DFT calculations, so the first path is excluded and the second path is more possible for the above process. These results strongly prove that O_2 is preferentially adsorbed on the photoinduced O_v, manifesting the photoinduced O_v behaves higher reactivity for O_2 chemisorption than conventional O_v and Cu single atom sites.

Afterward, the product of molecular oxygen activation was detected by in-situ Raman spectroscopy (Fig. 4e). Under irradiation, a new characteristic peak at about 800–820 cm^{-1} can be detected, assigned to monatomic oxygen ions (O^{-}) [36], and its content increases over time (Figure S32), indicating that adsorbed O_2 has been converted to powerful O^{-} species. Interestingly, this oxygen species cannot be observed on MnO$_2$ under irradiation (Figure S33) and Cu-MnO$_2$ under heating (Figure S34), verifying the essential role of Cu single atoms and light irradiation in O_2 activation. A further experiment was carried out to prove the origin of O^{-} species. In-situ Raman spectra on 0.5 Cu-MnO$_2$ in N_2 under irradiation (Figure S35) were recorded and show no O^{-} signal, excluding the possibility that the activation of O_{latt}^{2-} could produce O^{-} species. Besides, in the $^{18}O_2$ isotope-labeled experiment (Figure S30), if the source of O^{-} is O_{latt}^{2-}, the $^{16}O_2$ signal will not increase, at variance with the current results, further implying that O^{-} derives from O_2 rather than O_{latt}^{2-}. Additionally, the 1:1:1:1 quartet split signal of O_2^{-} appears in ESR spectra (Figure S36), but it is absent in in-situ Raman spectra, indicating that O_2^{-} can quickly turn into O^{-} during the activation process. The adsorbed O_2 could probably undergo the following transformation: $O_2 \rightarrow O_2^{-} \rightarrow O_2^{2-} \rightarrow O^{-} + O^{2-}$ [37,38], then generated O^{2-} repairs photoinduced O_v and the active O^{-} is responsible for the catalytic oxidation reaction.

Subsequently, in-situ FT-IR spectra were collected to disclose the effect of such O_2 activation induced by Cu single atom on reaction pathway of toluene oxidation. For MnO$_2$, the bands at 1587 and 1606 cm^{-1} are assigned to adsorbed toluene molecules [39,40] and their intensity obviously decreases, indicating the consumption/conversion of toluene (Fig. 5a). A series of oxidation products of -CH$_3$ group arise, including benzyl alcohol (-OH)[39,41–43], benzaldehyde (-CHO) and benzoic acid (-COOH). Benzaldehyde (1495, 1678 and 1723 cm^{-1}) accumulates [44,45], but the content of benzoic acid (1542, 1563 and 1631 cm^{-1}) is little [39,44], certifying the relatively poor activity of MnO$_2$. The band of maleates at 1294 cm^{-1} could verify the cleavage of benzene ring [45,46]. According to these intermediates, the reaction pathway of toluene oxidation on MnO$_2$ is speculated as follow: toluene → benzyl alcohol → benzaldehyde → benzoic acid → maleates → CO$_2$ + H$_2$O. On 0.5 Cu-MnO$_2$, the same intermediates are detected, indicating a negligible influence of Cu single atom on the reaction pathway of toluene oxidation. But it is noticeable for the enhanced quantity of intermediates, particularly benzoic acid and maleates (Fig. 5b). The new characteristic bands of benzoic acid (1388, 1406, 1426 and 1552 cm^{-1}) [44] and maleates (1786 and 1838 cm^{-1}) [47] can be discovered. Besides, notably, the band intensity of benzaldehyde at 1648–1688 cm^{-1} and benzoic acid at 1532–1552 cm^{-1} keeps decreasing in the first 20 min [39,45,48], and the consumption of maleates becomes more apparent than that on MnO$_2$. These results unveil the rapid transformation of intermediates, in favor of accelerating the release of active sites. Therefore, Cu single atoms can substantially facilitate O_2 activation to produce more active oxygen species, such as O^{-}, then remarkably promote the generation and transformation of intermediates. Meanwhile, the adsorption of intermediates on the Cu-MnO$_2$ catalyst surface was probed during catalytic reaction (Figure S37). Toluene and all intermediates, including benzyl alcohol, benzaldehyde, benzoic acid and maleates, are adsorbed on the Cu sites. Besides, it has been proven that O_2 is adsorbed on the photoinduced O_v. So, the spatial separation of the adsorption sites of O_2 and intermediates can be achieved, thus avoiding competitive adsorption between O_2 and

Fig. 5. In-situ FT-IR spectra of toluene oxidation on (a) MnO$_2$ and (b) 0.5 Cu-MnO$_2$ under irradiation in air (-OH: benzyl alcohol; -CHO: benzaldehyde; -COOH: benzoic acid). In-situ FT-IR spectra of toluene oxidation on 0.5 Cu-MnO$_2$ at 109 °C without irradiation in (c) N$_2$ and (d) air.

Scheme 1. Schematic illustration of enhanced molecular oxygen activation (MOA) by recyclable photoinduced Cu^{I}-O$_{v}$-Mn site.

intermediates on Cu single atom sites.

Thermocatalytic oxidation of toluene on 0.5 Cu-MnO$_2$ was explored, as displayed in Fig. 5c and d. All intermediates remain unchanged while switching N$_2$ to air, proving that surface lattice oxygen is the major active oxygen species of 0.5 Cu-MnO$_2$ for thermocatalysis, which is identical to that of MnO$_2$ based on our previous work [13]. It also suggests that the thermal effect can't motivate effective O$_2$ activation. And the absence of light significantly retards the formation of intermediates, further confirming its vital promoting role in O$_2$ activation.

These results have unlocked an efficient O$_2$ activation mechanism, as depicted in Scheme 1. First, photogenerated electron transfers from MnO$_2$ to Cu single atom site via the Cu^{II}-O-Mn bond, then electron localization at Cu^{II} site leads to its valence state variation (Cu^{2+}→Cu$^+$), accompanied by the generation of photoinduced O$_v$ to form Cu^{I}-O$_v$-Mn site. Next, O$_2$ is adsorbed on the photoinduced O$_v$ and activated by the photogenerated electron from Cu^{I} site. Subsequently, the valence of Cu reverts to +2 due to the consumption of photogenerated electrons and photoinduced O$_v$ is filled by O^{2-} from O$_2$ activation, accomplishing the regeneration of the Cu^{II}-O-Mn site. Finally, Cu single atom site will keep on this circulation with the co-assistance of photogenerated electron and O$_2$ molecule. The cooperation of photoinduced O$_v$ and sufficient charge transport can enhance O$_2$ activation capability to generate constant O$^-$ for oxidation reaction. The recyclable Cu^{I}-O$_v$-Mn site overcomes the bottlenecks of difficult regeneration of conventional O$_v$ and competitive adsorption of O$_2$ and reactants/intermediates on single atom sites, to accomplish continuous O$_2$ activation. Furthermore, the mode of O$_2$ activation has an obvious improvement. Compared to the general O$_2$ activation route on MnO$_2$, which only motivates O$_2$ by weakening O-O bond to produce O$_2^-$ (Figure S36), Cu^{I}-O$_v$-Mn site can realize direct O-O bond breakage to produce more reactive O$^-$ [49,50], thus achieving a higher increase of catalytic activity than that of MnO$_2$ under irradiation (Fig. 3a). Finally, this strategy is extended to other SACs with single atoms in easily-changed valence states, such as Co and Fe, due to their similar HOMO and LUMO energy levels of Cu-MnO$_2$, Co-MnO$_2$ and Fe-MnO$_2$ (Figure S38, S39 and Table S2).

Finally, the photothermal catalytic mechanism over Cu-MnO$_2$ catalyst can be shed light on. The superior photothermal catalytic performance derives from the synergy of light-driven thermocatalysis and photocatalysis. In the region of low temperature, photocatalysis is crucial and the Cu^{I}-O$_v$-Mn site can efficiently activate O$_2$ to produce reactive O$^-$ to degrade toluene. As temperature rises due to elevated light intensity, thermal enhancement can predominate and surface lattice oxygen is the key active species. At the same time, light can enhance the kinetics to achieve faster toluene elimination.

4. Conclusion

In summary, we have developed Cu-MnO$_2$ single-atom catalysts with a unique reversible evolution of Cu^{II}-O-Mn to Cu^{I}-O$_v$-Mn to accomplish excellent molecular oxygen activation (MOA) performance, thus remarkably enhancing the catalytic activity in O$_2$-involved oxidation reactions. Cu-MnO$_2$ catalysts achieved toluene conversion of as high as 96 % and ultra-high stability in over 70 days, rivaling the state-of-the-art supported Pt catalysts. The Cu^{II}-O-Mn sites can be recovered from Cu^{I}-O$_v$-Mn sites by O$_2$ molecule activation for the next-cycle. In contrast to conventional O$_v$ blockage by O$_2$ refilling, the photoinduced O$_v$ of Cu^{I}-O$_v$-Mn sites is renewable and possesses a stronger ability in MOA. The separation of electron-hole pairs is improved by Cu^{II}/Cu^{I} cycle to continuously supply adequate photogenerated electrons, thus rapid and sustained O$_2$ activation is guaranteed, and rich monatomic oxygen ions (O$^-$) are produced as active oxygen species for oxidation reactions. The present strategy of MOA is also different from previously reported O$_2$ activation by single atom sites, on which competitive adsorption between O$_2$ and reactants/intermediates usually happens. Beyond that, the new Cu^{I}-O$_v$-Mn sites can break the routine, which only elongates O-O bond by electron transfer, and forthrightly cut O-O bond to generate

strong-oxidizing O$^-$. The novel O$_2$ activation mechanism elucidated here will widen the fundamental understanding of MOA and inspire the development of novel and highly efficient oxidation catalysts.

CRediT authorship contribution statement

Min Wang: Investigation. **Xixiong Jin:** Investigation, Funding acquisition. **Yang Wang:** Writing – review & editing, Writing – original draft, Methodology, Investigation, Conceptualization. **Lina Li:** Writing – review & editing, Resources, Methodology. **Lingxia Zhang:** Writing – review & editing, Writing – original draft, Supervision, Resources, Methodology, Funding acquisition, Conceptualization. **Bohan A:** Investigation. **Bing Nan:** Investigation. **Jianlin Shi:** Writing – review & editing, Supervision, Resources, Methodology.

Declaration of Competing Interest

The authors declare that they have no known competing financial interests or personal relationships that could have appeared to influence the work reported in this paper.

Data availability

Data will be made available on request.

Acknowledgment

Appendix A. Supporting information

Supplementary data associated with this article can be found in the online version at doi:10.1016/j.apcatb.2024.124110.

References

[1] A. Rushiti, C. Hattig, Activation of molecular O$_2$ on CoFe$_2$O$_4$ (001) surfaces: an embedded cluster study, Chem. Eur. J. 27 (2021) 17115–17126.

[2] Z. Wang, M. Cheng, Y. Liu, Z. Wu, H. Gu, Y. Huang, L. Zhang, X. Liu, Dual-atomic-site catalysts for molecular oxygen activation in heterogeneous thermo-/electro-catalysis, Angew. Chem. Int. Ed. 62 (2023).

[3] Q. Li, F.-t Li, Recent advances in molecular oxygen activation via photocatalysis and its application in oxidation reactions, Chem. Eng. J. 421 (2021).

[4] C. Pan, C. Wang, X. Zhao, P. Xu, F. Mao, J. Yang, Y. Zhu, R. Yu, S. Xiao, Y. Fang, H. Deng, Z. Luo, J. Wu, J. Li, S. Liu, S. Xiao, L. Zhang, Y. Guo, Neighboring sp-hybridized carbon participated molecular oxygen activation on the interface of sub-nanocluster CuO/graphdiyne, J. Am. Chem. Soc. 144 (2022) 4942–4951.

[5] Y. Shi, Z. Yang, L. Shi, H. Li, X. Liu, X. Zhang, J. Cheng, C. Liang, S. Cao, F. Guo, X. Liu, Z. Ai, L. Zhang, Surface boronizing can weaken the excitonic effects of BiOBr nanosheets for efficient O$_2$ activation and selective NO oxidation under visible light irradiation, Environ. Sci. Technol. 56 (2022) 14478–14486.

[6] K.C. Qian, L.L. Du, X.H. Zhu, S.P. Liang, S. Chen, H. Kobayashi, X.Q. Yan, M. Xu, Y. H. Dai, R.H. Li, Directional oxygen activation by oxygen-vacancy-rich WO$_2$ nanorods for superb hydrogen evolution via formaldehyde reforming, J. Mater. Chem. A 7 (2019) 14592–14601.

[7] Y.F. Zheng, K.X. Fu, Z.H. Yu, Y. Su, R. Han, Q.L. Liu, Oxygen vacancies in a catalyst for VOCs oxidation: synthesis, characterization, and catalytic effects, J. Mater. Chem. A 10 (2022) 14171–14186.

[8] Z.H. Xue, D.Y. Luan, H.B. Zhang, X.W. Lou, Single-atom catalysts for photocatalytic energy conversion, Joule 6 (2022) 92–133.

[9] A. Beniya, S. Higashi, Towards dense single-atom catalysts for future automotive applications, Nat. Catal. 2 (2019) 590–602.

[10] U.J. Etim, P. Bai, O.M. Gazit, Z.Y. Zhong, Low-temperature heterogeneous oxidation catalysis and molecular oxygen activation, Catal. Rev. 65 (2023) 239–425.

[11] Y.R. Fang, Q. Zhang, H. Zhang, X.M. Li, W. Chen, J. Xu, H. Shen, J. Yang, C.A. Q. Pan, Y.H. Zhu, J.L. Wang, Z. Luo, L.M. Wang, X.D. Bai, F. Song, L.Z. Zhang, Y. B. Guo, Dual activation of molecular oxygen and surface lattice oxygen in single atom Cu$_1$/TiO$_2$ catalyst for CO oxidation, Angew. Chem. Int. Ed. 61 (2022).

[12] H.Y. Gu, X. Liu, X.F. Liu, C.C. Ling, K. Wei, G.M. Zhan, Y.B. Guo, L.Z. Zhang, Adjacent single-atom irons boosting molecular oxygen activation on MnO$_2$, Nat. Commun. 12 (2021).

[13] Y. Wang, J. Dai, M. Wang, F. Qi, X. Jin, L. Zhang, Enhanced toluene oxidation by photothermal synergetic catalysis on manganese oxide embedded with Pt single-atoms, J. Colloid Interface Sci. 636 (2023) 577–587.

[14] M. Dolg, U. Wedig, H. Stoll, H. Preuss, Energy-adjusted ab initio pseudopotentials for the first row transition elements, J. Chem. Phys. 86 (1987) 866–872.

[15] J.P. Perdew, K. Burke, M. Ernzerhof, Generalized gradient approximation made simple, Phys. Rev. Lett. 77 (1996) 3865–3868.

[16] K. Li, N. Li, N.N. Yan, T.Y. Wang, Y.T. Zhang, Q. Song, H.J. Li, Adsorption of small hydrocarbons on pristine, N-doped and vacancy graphene by DFT study, Appl. Surf. Sci. 515 (2020).

[17] Y.J. Shen, J. Deng, L.P. Han, W. Ren, D.S. Zhang, Low-temperature combustion of toluene over Cu-doped $SmMn_2O_5$ mullite catalysts via creating highly active Cu^{2+}-O-Mn^{4+} sites, Environ. Sci. Technol. (2022).

[18] D. Li, Y. Zhao, Y. Miao, C. Zhou, L.P. Zhang, L.Z. Wu, T. Zhang, Accelerating electron-transfer dynamics by TiO_2-immobilized reversible single-atom copper for enhanced artificial photosynthesis of urea, Adv. Mater. 34 (2022) e2207793.

[19] J.N. Nian, S.A. Chen, C.C. Tsai, H.S. Teng, Structural feature and catalytic performance of Cu species distributed over TiO_2 nanotubes, J. Phys. Chem. B 110 (2006) 25817–25824.

[20] L. Yuan, S.F. Hung, Z.R. Tang, H.M. Chen, Y.J. Xiong, Y.J. Xu, Dynamic evolution of atomically dispersed Cu species for CO_2 photoreduction to solar fuels, ACS Catal. 9 (2019) 4824–4833.

[21] Y.L. Guo, M.C. Wen, S.N. Song, Q.X. Liu, G.Y. Li, T.C. An, Enhanced catalytic elimination of typical VOCs over ZnCoO catalyst derived from in situ pyrolysis of ZnCo bimetallic zeolitic imidazolate frameworks, Appl. Catal. B 308 (2022).

[22] C.Y. Chen, Q.M. Wu, F. Chen, L. Zhang, S.X. Pan, C.Q. Bian, X.M. Zheng, X.J. Meng, F.S. Xiao, Aluminium-rich Beta zeolite-supported platinum nanoparticles for the low-temperature catalytic removal of toluene, J. Mater. Chem. A 3 (2015) 5556–5562.

[23] T. Gan, X.F. Chu, H. Qi, W.X. Zhang, Y.C. Zou, W.F. Yan, G. Liu, Pt/Al_2O_3 with ultralow Pt-loading catalyze toluene oxidation: promotional synergistic effect of Pt nanoparticles and Al_2O_3 support, Appl. Catal. B 257 (2019).

[24] X. Min, M.M. Guo, L.Z. Liu, L. Li, J.N. Gu, J.X. Liang, C. Chen, K. Li, J.P. Jia, T. H. Sun, Synthesis of MnO_2 derived from spent lithium-ion batteries via advanced oxidation and its application in VOCs oxidation, J. Hazard. Mater. 406 (2021).

[25] Y. Wang, K.S. Liu, J. Wu, Z.M. Hu, L. Huang, J. Zhou, T. Ishihara, L.M. Guo, Unveiling the effects of alkali metal ions intercalated in layered MnO_2 for formaldehyde catalytic oxidation, ACS Catal. 10 (2020) 10021–10031.

[26] L. Liu, H. Huang, F. Chen, H. Yu, N. Tian, Y. Zhang, T. Zhang, Cooperation of oxygen vacancies and 2D ultrathin structure promoting CO_2 photoreduction performance of $Bi_4Ti_3O_{12}$, Sci. Bull. 65 (2020) 934–943.

[27] B.B. Chen, B. Wu, L.M. Yu, M. Crocker, C. Shi, Investigation into the catalytic roles of various oxygen species over different crystal phases of MnO_2 for C_6H_6 and HCHO oxidation, ACS Catal. 10 (2020) 6176–6187.

[28] Y. Wang, D.Y. Yang, S.Z. Li, L.X. Zhang, G.Y. Zheng, L.M. Guo, Layered copper manganese oxide for the efficient catalytic CO and VOCs oxidation, Chem. Eng. J. 357 (2019) 258–268.

[29] D. Delimaris, T. Ioannides, VOC oxidation over CuO-CeO_2 catalysts prepared by a combustion method, Appl. Catal. B 89 (2009) 295–302.

[30] W.J. Xu, X. Chen, J. Chen, H.P. Jia, Bimetal oxide CuO/Co_3O_4 derived from Cu ions partly-substituted framework of ZIF-67 for toluene catalytic oxidation, J. Hazard. Mater. 403 (2021).

[31] X.X. Li, Y.R. Wang, D.Y. Chen, N.J. Li, Q.F. Xu, H. Li, J.H. He, J.M. Lu, A highly dispersed Pt/copper modified-MnO_2 catalyst for the complete oxidation of volatile organic compounds: the effect of oxygen species on the catalytic mechanism, Green Energy Environ. 8 (2023) 538–547.

[32] S. Yang, Z.T. Qi, Y.C. Wen, X.X. Wang, S.H. Zhang, W. Li, S.J. Li, Generation of abundant oxygen vacancies in Fe doped δ-MnO_2 by a facile interfacial synthesis strategy for highly efficient catalysis of VOCs oxidation, Chem. Eng. J. 452 (2023).

[33] L. Luo, Z. Gong, Y. Xu, J. Ma, H. Liu, J. Xing, J. Tang, Binary Au-Cu reaction sites decorated ZnO for selective methane oxidation to C1 oxygenates with nearly 100% selectivity at room temperature, J. Am. Chem. Soc. 144 (2022) 740–750.

[34] S.J. Feng, T. Wang, B. Liu, C.L. Hu, L.L. Li, Z.J. Zhao, J.L. Gong, Enriched surface oxygen vacancies of photoanodes by photoetching with enhanced charge separation, Angew. Chem. Int. Ed. 59 (2020) 2044–2048.

[35] T.L. Thompson, J.T. Yates, Surface science studies of the photoactivation of TiO_2-new photochemical processes, Chem. Rev. 106 (2006) 4428–4453.

[36] Q.Y. Lian, L.L. Hu, D.R. Ma, Y.M. Jiao, D.H. Xia, Y.J. Huang, Z.Y. Tang, W. Qu, H. N. Zhao, C. He, D.D. Gang, Interstitial atomic Bi charge-alternating processor boosts twofold molecular oxygen activation enabling rapid catalytic oxidation reactions at room temperature, Adv. Funct. Mater. 32 (2022).

[37] Z. Wu, M. Li, J. Howe, H.M. Meyer 3rd, S.H. Overbury, Probing defect sites on CeO_2 nanocrystals with well-defined surface planes by Raman spectroscopy and O_2 adsorption, Langmuir 26 (2010) 16595–16606.

[38] V.V. Pushkarev, V.I. Kovalchuk, J.L. d'Itri, Probing defect sites on the CeO_2 surface with dioxygen, J. Phys. Chem. B 108 (2004) 5341–5348.

[39] S. Mo, J. Li, R. Liao, P. Peng, J. Li, J. Wu, M. Fu, L. Liao, T. Shen, Q. Xie, D. Ye, Unraveling the decisive role of surface CeO_2 nanoparticles in the Pt-CeO_2/MnO_2 hetero-catalysts for boosting toluene oxidation: synergistic effect of surface decorated and intrinsic O-vacancies, Chem. Eng. J. 418 (2021).

[40] F. Wang, J. Deng, S. Impeng, Y. Shen, T. Yan, G. Chen, L. Shi, D. Zhang, Unraveling the effects of the coordination number of Mn over α-MnO_2 catalysts for toluene oxidation, Chem. Eng. J. 396 (2020).

[41] A. Aguirre, E.L. Fornero, A. Villarreal, S.E. Collins, Identification of key reaction intermediates during toluene combustion on a Pd/CeO_2 catalyst using operando modulated DRIFT spectroscopy, Catal. Today 394 (2022) 225–234.

[42] J.P. Zhong, Y.K. Zeng, M.Y. Zhang, W.H. Feng, D.R. Xiao, J.L. Wu, P.R. Chen, M. L. Fu, D.Q. Ye, Toluene oxidation process and proper mechanism over Co_3O_4 nanotubes: Investigation through in-situ DRIFTS combined with PTR-TOF-MS and quasi in-situ XPS, Chem. Eng. J. (2020) 397.

[43] L.C. Chen, P. Chen, H. Wang, W. Cui, J.P. Sheng, J.Y. Li, Y.X. Zhang, Y. Zhou, F. Dong, Surface lattice oxygen activation on $Sr_2Sb_2O_7$ enhances the photocatalytic mineralization of toluene: from reactant activation, intermediate conversion to product desorption, ACS Appl. Mater. Interfaces 13 (2021) 5153–5164.

[44] J. Li, R. Chen, W. Cui, Xa Dong, H. Wang, K.-H. Kim, Y. Chu, J. Sheng, Y. Sun, F. Dong, Synergistic photocatalytic decomposition of a volatile organic compound mixture: high efficiency, reaction mechanism, and long-term stability, ACS Catal. 10 (2020) 7230–7239.

[45] W. Yang, Y. Peng, Y. Wang, Y. Wang, H. Liu, Za Su, W. Yang, J. Chen, W. Si, J. Li, Controllable redox-induced in-situ growth of MnO_2 over Mn_2O_3 for toluene oxidation: active heterostructure interfaces, Appl. Catal. B 278 (2020).

[46] Z. Wang, H. Yang, R. Liu, S. Xie, Y. Liu, H. Dai, H. Huang, J. Deng, Probing toluene catalytic removal mechanism over supported Pt nano- and single-atom-catalyst, J. Hazard. Mater. 392 (2020), 122258-122258.

[47] S.P. Mo, Q. Zhang, J.Q. Li, Y.H. Sun, Q.M. Ren, S.B. Zou, Q. Zhang, J.H. Lu, M. L. Fu, D.Q. Mo, J.L. Wu, H.M. Huang, D.Q. Ye, Highly efficient mesoporous MnO_2 catalysts for the total toluene oxidation: oxygen-Vacancy defect engineering and involved intermediates using in situ drifts, Appl. Catal. B 264 (2020).

[48] L.L. Zhao, Z.P. Zhang, Y.S. Li, X.S. Leng, T.R. Zhang, F.L. Yuan, X.Y. Niu, Y.J. Zhu, Synthesis of Ce_aMnO_x hollow microsphere with hierarchical structure and its excellent catalytic performance for toluene combustion, Appl. Catal. B 245 (2019) 502–512.

[49] M.M. Montemore, M.A. van Spronsen, R.J. Madix, C.M. Friend, O_2 activation by metal surfaces: implications for bonding and reactivity on heterogeneous catalysts, Chem. Rev. 118 (2018) 2816–2862.

[50] Z. Yang, Z. Shi, H. Li, C. Mao, X. Wang, X. Liu, X. Liu, L. Zhang, Oxygen and chlorine dual vacancies enable photocatalytic O_2 dissociation into monatomic reactive oxygen on BiOCl for refractory aromatic pollutant removal, Environ. Sci. Technol. 56 (2022) 3587–3595.